







Field-tunable Weyl points and large anomalous Hall effect in the degenerate magnetic semiconductor EuMg_2Bi_2

M. Kondo ^{1,*}, M. Ochi,^{1,2} R. Kurihara,^{3,4} A. Miyake ³, Y. Yamasaki,^{5,6} M. Tokunaga ³, H. Nakao ⁷, K. Kuroki,¹ T. Kida ⁸, M. Hagiwara,⁸ H. Murakawa,¹ N. Hanasaki,^{1,9} and H. Sakai ^{1,†}

¹Department of Physics, Osaka University, Toyonaka, Osaka 560-0043, Japan

²Forefront Research Center, Osaka University, Toyonaka, Osaka 560-0043, Japan

³The Institute for Solid State Physics, The University of Tokyo, Kashiwa, Chiba 277-8581, Japan

⁴Department of Physics, Faculty of Science and Technology, Tokyo University of Science, Noda, Chiba 278-8510, Japan

⁵Research and Services Division of Materials Data and Integrated System (MaDIS), National Institute for Materials Science (NIMS), Tsukuba, Ibaraki 305-0047, Japan

⁶Center for Emergent Matter Science (CEMS), RIKEN, Wako, Saitama 351-0198, Japan

⁷Photon Factory, Institute of Materials Structure Science, KEK, Tsukuba, Ibaraki 305-0801, Japan

⁸Center for Advanced High Magnetic Field Science (AHMF), Graduate School of Science, Osaka University, Toyonaka, Osaka 560-0043, Japan

⁹Spintronics Research Network Division, Institute for Open and Transdisciplinary Research Initiatives, Osaka University, Suita, Osaka 565-0871, Japan



(Received 25 July 2022; revised 2 December 2022; accepted 8 March 2023; published 28 March 2023)

Magnets, with topologically nontrivial Dirac/Weyl points, have recently attracted significant attention owing to their unconventional physical properties, such as a large anomalous Hall effect. However, they typically have a high carrier density and a complicated band structure near the Fermi energy. In this Letter, we report a degenerate magnetic semiconductor EuMg_2Bi_2 , which exhibits a single valley at the Γ point, where field-tunable Weyl points form via a magnetic exchange interaction with the local Eu spins. By the high-field measurements on high-quality single crystals, we observed quantum oscillations in the resistivity, elastic constant, and surface impedance, which enabled us to determine the position of the Fermi energy E_F . In combination with a first-principles calculation, we revealed that the Weyl points are located in the vicinity of E_F when the Eu spins are fully polarized, leading to a peak of energy-dependent anomalous Hall conductivity due to the Berry curvature. Accordingly, in the forced ferromagnetic phase, we observed a large anomalous Hall effect (Hall angle $\Theta_{\text{AH}} \sim 0.07$) qualitatively consistent with the calculation, which demonstrates a marked impact of the Weyl points in the simple band structure.

DOI: [10.1103/PhysRevB.107.L121112](https://doi.org/10.1103/PhysRevB.107.L121112)

The interplay of magnetism and topology is one of the most active research topics in recent condensed matter physics. A magnetic Weyl semimetal or Weyl magnet is a typical topological magnet, in which spin-polarized linear bands cross in the vicinity of the Fermi energy, thereby forming topologically protected crossing points (Weyl points). Since the large Berry curvature originating from the Weyl points leads to exotic physical properties [1] such as giant anomalous Hall/Nernst effects (AHE/ANE) and chiral anomalies, the exploration of Weyl magnets is important not only for basic science but also for device applications. To date, a number of Weyl magnets have been predicted and their experimental verifications are currently in progress. Typical examples include antiferromagnets with noncollinear magnetic structures [e.g., $\text{Mn}_3(\text{Sn}, \text{Ge})$ [2–7]] and ferromagnets with peculiar crystal structures such as kagome and Heusler lattices [e.g., $\text{Co}_3\text{Sn}_2\text{S}_2$ [8–11], Fe_3GeTe_2 [12,13],

$\text{Co}_2\text{Mn}(\text{Al}, \text{Ga})$ [14–18]]. These metallic magnets generally exhibit complicated band structures with many topologically trivial bands near the Fermi energy.

Another way to obtain a Weyl magnet involves using magnetic interactions in semimetals or narrow-gap semiconductors with a partial substitution of magnetic elements (e.g., Eu^{2+} , Gd^{3+}) acting as localized spins. In this case, given that Weyl points are formed by the exchange splitting of the bands due to the (field-induced) magnetization, materials with much simpler band structures can be considered as candidates. As typical examples, in GdPtBi [19,20], EuTiO_3 [21], $\text{EuCd}_2(\text{As}, \text{Sb})_2$ [22–27], and $\alpha\text{-EuP}_3$ [28], various unconventional AHEs associated with field-induced Weyl points have been recently reported. However, in most of them, both the conduction and valence bands cross in a complex manner owing to the semimetallic nature, leading to multiple Weyl points at various energies. To investigate the physics of Weyl magnets, materials with fewer bands involved in forming the Weyl points are more promising.

We here are focused on the XMg_2Bi_2 compound ($X = \text{Ca}, \text{Sr}, \text{Ba}, \text{Eu}, \text{and Yb}$) [29–35]. This compound exhibits

*Corresponding author: kondo@gmr.phys.sci.osaka-u.ac.jp

†Corresponding author: sakai@phys.sci.osaka-u.ac.jp

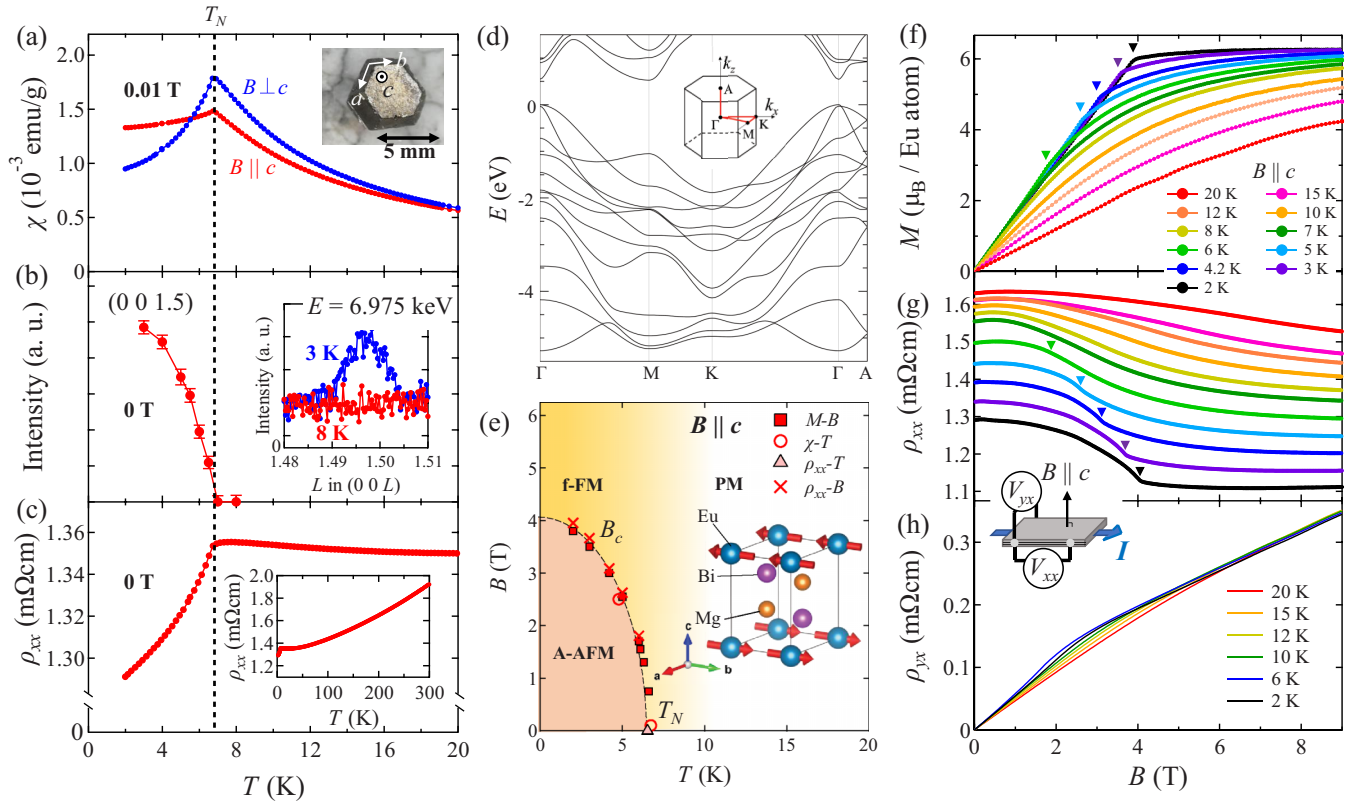


FIG. 1. (a) Temperature dependence of out-of-plane (red) and in-plane (blue) magnetic susceptibilities measured at 0.01 T in a cooling run. The vertical dotted line denotes the Néel temperature T_N ($=6.7$ K) for the Eu sublattice. The inset shows a photograph of a typical crystal. (b) Temperature dependence of intensity of resonant magnetic reflection (0 0 1.5) at $E = 6.975$ keV at 0 T. The inset shows the intensities of (0 0 1.5) magnetic reflection below and above T_N (3 and 8 K, respectively). (c) The temperature dependence of in-plane resistivity ρ_{xx} below 20 K. The inset shows the overall temperature dependence of ρ_{xx} . (d) Calculated band structure of EuMg₂Bi₂ for the A-type antiferromagnetic order of Eu spins. The inset shows the first Brillouin zone. (e) The magnetic phase diagram of EuMg₂Bi₂ as functions of the field ($B \parallel c$) and temperature (T). PM, A-AFM, and f-FM denote the paramagnetic, A-type antiferromagnetic, and forced-ferromagnetic phases, respectively. B_c corresponds to the transition field to the f-FM phase. The inset exhibits the crystal and magnetic structure of EuMg₂Bi₂. The easy-axis direction is here assumed to be parallel to the b axis because the in-plane spin direction cannot be determined from the present experiment on a sample with magnetic domains [35] (see Fig. S2 for details). (f)–(h) The field dependence of (f) magnetization M , (g) ρ_{xx} , and (h) Hall resistivity ρ_{yx} (up to 9 T). Triangles in (f) and (g) denote B_c at various temperatures below T_N . All ρ_{xx} data in (g) are shifted vertically by 20 or 40 $\mu\Omega\text{cm}$ for clarity. The insets show a schematic illustration of measurements of $\rho_{xx}(V_{xx})$ and $\rho_{yx}(V_{yx})$.

a CaAl₂Si₂-type crystal structure [space group $P\bar{3}m1$; see Fig. 1(e) inset], which corresponds to an alternative stacking of the X layer with a triangular lattice and a Mg₂Bi₂ layer with a buckled honeycomb lattice. A previous first-principles calculation predicted that the valence band top and conduction band bottom, mainly consisting of Mg s and Bi p orbitals, are located at the Γ point and no other bands exist near the Fermi energy [30,31]. Furthermore, it was highlighted that the band gap (and possible band inversion) is tunable with the X species. Recent angle-resolved photoemission spectroscopy (ARPES) experiments indeed revealed a signature of a transition from a band insulator to a Dirac semimetal via the replacement of the X site from Sr to Ba [32]. Hence, this type of band structure, which is sensitive to the X sites, should also be significantly modified via the exchange interaction, when the nonmagnetic X site is substituted with a magnetic Eu²⁺ ion. Moreover, the zero-field band structure for EuMg₂Bi₂ examined by ARPES shows a single small hole pocket around the Γ point [33], consisting only of valence bands. This likely provides an ideal

arena to reveal the impact of Weyl points without considering many different kinds of bands. It was previously reported that EuMg₂Bi₂ undergoes antiferromagnetic order below ~ 6.7 K at zero magnetic field [34,35]. However, the variation of the band structure with respect to the magnetic states of Eu spins and associated magnetotransport phenomena has been elusive.

In this Letter, by a detailed transport measurement and first-principles calculation, we show the band structure to be dependent on the magnetic order for EuMg₂Bi₂. Specifically, we observed a clear quantum oscillation originating from the bulk band at high fields (up to 55 T), which enabled us to experimentally determine the Fermi energy. Hence, it was clarified that the Weyl points are located in the vicinity of the Fermi energy, when Eu spins are fully polarized. In experiments, we observed a large AHE in the forced ferromagnetic phase, which was comparable in magnitude to those reported for ferromagnetic Weyl (semi)metals. We discuss its origin by comparing with the calculation based on the Berry curvature mechanism relevant to the emergent Weyl points.

Single crystals of EuMg_2Bi_2 were grown via a self-flux method [29] with a starting composition of $\text{EuMg}_8\text{Bi}_{10}$. Large single crystals with a typical size corresponding to $5 \times 5 \times 5 \text{ mm}^3$ were obtained [see the inset of Fig. 1(a)]. Resonant x-ray magnetic diffraction measurements near the Eu L_3 absorption edge ($E = 6.975 \text{ keV}$) were performed at BL-3A in Photon Factory, KEK, Japan. The low-field resistivity and magnetization were measured using a physical property measurement system (PPMS, Quantum Design) and a magnetic property measurement system (MPMS, Quantum Design). The high-field resistivity measurements were performed up to 55 T using the nondestructive midpulse magnet at the International MegaGauss Science Laboratory at the Institute for Solid State Physics, University of Tokyo. To observe the quantum oscillations, we measured the surface impedance and elastic constant using a tunnel-diode oscillator (TDO) [36] and an ultrasonic pulse-echo method [37], respectively. We performed first-principles band-structure calculations using the Heyd-Scuseria-Ernzerhof (HSE06) energy functional [38] and projector augmented-wave methods [39] including the $+U$ correction [40,41] with $U_{\text{eff}} \equiv U - J = 14 \text{ eV}$ for the Eu- f orbitals [42] and the spin-orbit coupling, as implemented in the Vienna *ab initio* simulation package [43–46]. The band structures with spin polarization $\langle S_z \rangle$ were calculated using the Bi- p Wannier orbitals [47,48] extracted with the WANNIER90 software [49]. For details, see Supplemental Material [50].

Figure 1(a) shows the temperature dependence of the magnetic susceptibility, where a cusplike anomaly is discernible at $T_N = 6.7 \text{ K}$, indicating an antiferromagnetic transition of the Eu sublattice. While the magnetic susceptibility in $B \parallel c$ is almost constant below T_N , that for $B \perp c$ decreases significantly below T_N . This suggests that the easy axis of magnetization of Eu spins is within the ab plane. To investigate the order structure of Eu spins in the ground state, we performed a resonant x-ray magnetic scattering measurement. As shown in the inset of Fig. 1(b), a superlattice reflection (0 0 1.5) is observed below T_N , resonating at the Eu L_3 absorption edge $E = 6.975 \text{ keV}$ [57,58] [see Fig. S2(a) for details]. Since the intensity of this peak develops significantly below T_N [Fig. 1(b)], it arises from the magnetic reflection due to the Eu spin order. Furthermore, a q vector of (0 0 0.5) indicates that the Eu spins show A-type antiferromagnetic (A-AFM) order with a cell doubling along the c -axis direction. This result is consistent with previous neutron diffraction experiments at zero field [35,59]. By considering the anisotropy of magnetic susceptibility, the order structure of Eu spins is determined as shown in the inset of Fig. 1(e).

Figure 1(d) shows the band structure of EuMg_2Bi_2 in the A-AFM phase calculated using the HSE06 functional, which shows a direct band gap $E_g \sim 0.5 \text{ eV}$ at the Γ point. This semiconducting band structure is similar to that calculated for XMg_2Bi_2 ($X = \text{Sr}, \text{Ba}$) [31,32]. However, the metallic conduction was experimentally observed from room temperature to 20 K [inset to Fig. 1(c)], thereby indicating that a few carriers are present in reality. As shown in Fig. 1(c), the in-plane resistivity ρ_{xx} slowly increases with decreasing temperature below 20 K, followed by a rapid decrease below $T_N = 6.7 \text{ K}$. Thus, doped carriers are strongly coupled with the antiferromagnetic order (and fluctuation) of the Eu spins.

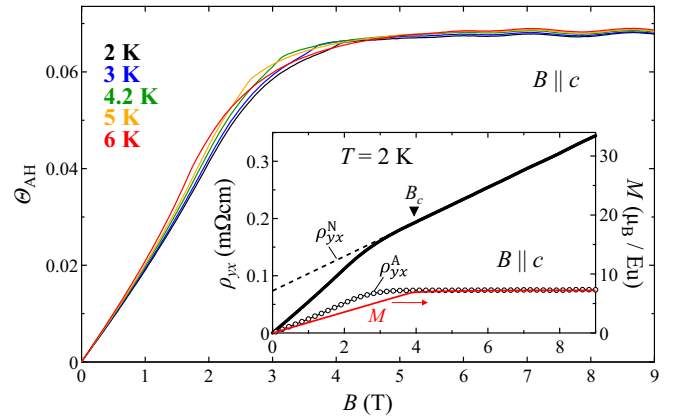


FIG. 2. Field dependence of anomalous Hall angle $\Theta_{\text{AH}} = \rho_{\text{yx}}^{\text{AH}}/\rho_{\text{xx}}$ at various temperatures. The oscillatory structure above 6 T is due to SdH oscillation for ρ_{yx} . The inset shows the field dependence of ρ_{yx} and its anomalous part $\rho_{\text{yx}}^{\text{A}}$ at 2 K. The black dotted line corresponds to the ordinary part $\rho_{\text{yx}}^{\text{N}}$ of ρ_{yx} at 2 K, which is obtained from the linear fit to the experimental data above B_c . Note here that the $\rho_{\text{yx}}^{\text{N}}$ is vertically shifted to demonstrate the fitted result at the high-field region. The red curve represents the field dependence of the magnetization M at 2 K.

To investigate the coupling between the magnetism and transport properties, we applied the field along the c axis to measure the magnetization and resistivity. Figure 1(f) shows the field dependence of magnetization M below 20 K. At 2 K, M increases almost linearly with increasing field up to $B_c = 3.9 \text{ T}$, above which M is almost constant, and Eu spins are fully polarized along the c axis. The saturated magnetization in this forced ferromagnetic (f-FM) phase is $M_{\text{sat}} \sim 6.1 \mu_{\text{B}}/\text{Eu}$, which is close to the magnetic moment of a bare Eu^{2+} ion. This indicates that the Eu $4f$ electrons are almost localized. As temperature increases, B_c shifts to lower magnetic fields and disappears above T_N . The resultant magnetic phase diagram is shown in Fig. 1(e).

Figure 1(g) shows the field dependence of ρ_{xx} below 20 K for $B \parallel c$. At 2 K, a negative magnetoresistance was observed for $B < B_c$. A clear kink is discernible at B_c , above which ρ_{xx} is almost constant up to 9 T. As temperature increases, B_c shifts to lower magnetic fields and the kink becomes less apparent. Figure 1(h) shows the magnetic field dependence of the Hall resistivity ρ_{yx} for $B \parallel c$. The positive slope of ρ_{yx} indicates that hole carriers are slightly doped, and thus E_F crosses the top of the valence band at the Γ point. Although ρ_{yx} is almost linear with respect to field above T_N , it deviates from the straight line below T_N ; a hump structure at approximately 2.5 T becomes pronounced as temperature decreases. This signals the evolution of AHE coupled with Eu magnetic ordering.

To extract the anomalous component $\rho_{\text{yx}}^{\text{A}}$, we estimate the ordinary component $\rho_{\text{yx}}^{\text{N}} = R_{\text{H}}B$ from the data above B_c , where the magnetization is fully saturated [Fig. 1(f)] [60]. As shown in the inset to Fig. 2, the Hall coefficient R_{H} is unambiguously determined at 2 K from the slope of ρ_{yx} above B_c . The resultant $\rho_{\text{yx}}^{\text{A}} = \rho_{\text{yx}} - \rho_{\text{yx}}^{\text{N}}$ is roughly proportional to magnetization (inset to Fig. 2) [61]. Figure 2 shows the field dependence

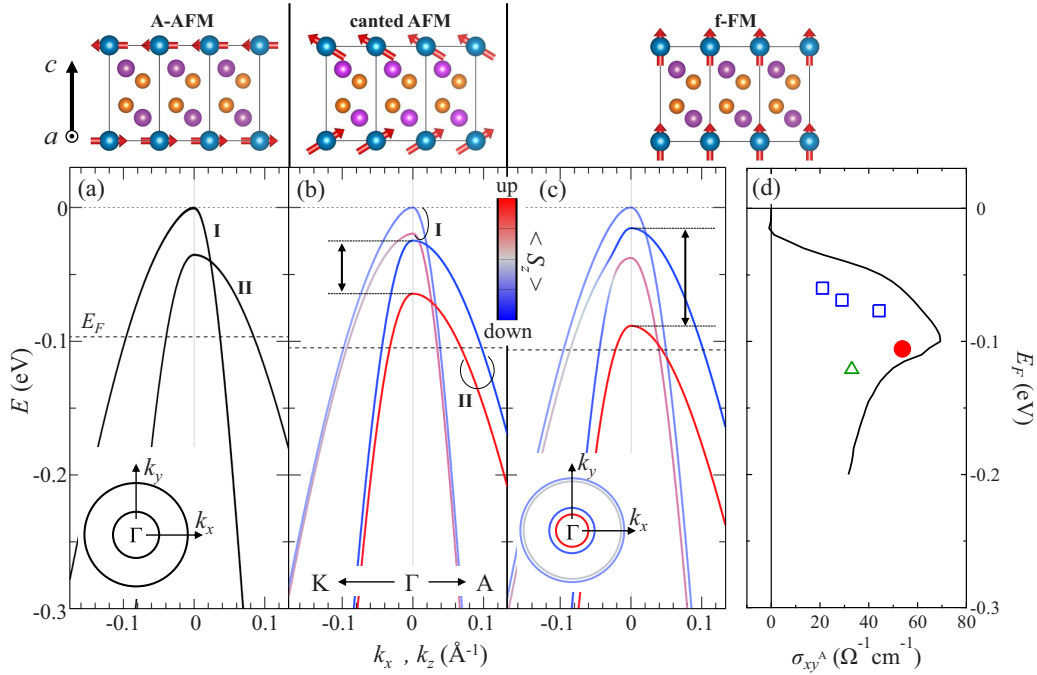


FIG. 3. (a)–(c) Valence band structures around the Γ point near E_F (lower panels) for various magnetic states (upper panels). Red and blue colors of band dispersions represent spin up and spin down, respectively. The dotted lines denote the Fermi energy E_F determined from the SdH frequency B_F at $T = 1.4$ K. The vertical arrows in (b) and (c) denote the size of spin splitting. The insets of (a) and (c) show the schematic illustration of Fermi surfaces within the $k_x k_y$ plane, where the color denotes the $\langle S_z \rangle$ value. (d) Anomalous Hall conductivity σ_{xy}^A as a function of E_F . The solid black curve represents the calculated result for the f-FM phase. The solid red circle denotes the experimental data (2 K, 9 T) for pristine EuMg_2Bi_2 , while the open blue squares and open green triangle denote those for the Mg-annealed crystals and In-doped crystal (see Fig. S9 for details), respectively.

of the anomalous Hall angle $\Theta_{\text{AH}} = \sigma_{xy}^A / \sigma_{xx}$ below T_N , where $\sigma_{xx} = \rho_{xx} / (\rho_{xx}^2 + \rho_{yx}^2)$ is longitudinal conductivity and $\sigma_{xy}^A = \rho_{yx}^A / (\rho_{xx}^2 + \rho_{yx}^2)$ is anomalous Hall conductivity (see Fig. S3 for determining ρ_{yx}^A at each temperature). At $B > B_c$, the Θ_{AH} is nearly constant (~ 0.07), reflecting the field dependence of magnetization. The constant value of Θ_{AH} is comparable to those reported for ferromagnetic Weyl semimetals $\text{Co}_3\text{Sn}_2\text{S}_2$ (~ 0.2 at 150 K) [8], Fe_3GeTe_2 (~ 0.09 at 2 K) [12], and GdPtBi (~ 0.15 at 2.5 K) [20]. Hence, such a large Θ_{AH} indicates that EuMg_2Bi_2 has band crossing points near E_F in the f-FM phase as a source of Berry curvature [62,63]. Below, by taking advantage of the simple band structure with a single valley [Fig. 1(d)], we compare the experimental and theoretical results in detail and reveal that the AHE in EuMg_2Bi_2 can be quantitatively explained by the intrinsic Berry curvature mechanism.

To clarify the impact of Eu spins on the band structure, we performed a first-principles band calculation for various magnetic states. We show the variation of valence bands near the Γ point in Figs. 3(a)–3(c). In the A-AFM phase (at zero field), there are two valence bands I and II consisting of Mg- s and Bi- p orbitals, which cross each other at $k_z \sim 0.03 \text{ \AA}^{-1}$ on the $\Gamma - A$ line [Fig. 3(a)]. This leads to a Dirac-like point because the crossing bands are spin degenerate in the A-AFM phase with no net magnetization. When the field is applied along the c axis, Eu spins start to cant towards the c axis. In Fig. 3(b), we show the band structure calculated for the Eu spins tilted by approximately 30° with respect to the ab

plane [upper panel of Fig. 3(b)]. In this canted AFM phase, the net magnetization from the Eu spins is no longer zero, which leads to clear spin splitting (red and blue) in bands I and II owing to the exchange interaction [21,28,64]. This leads to multiple Weyl-like points, where the spin-polarized bands cross. The magnitude of splitting increases as the field or the net magnetization along the c axis increases [vertical arrows in Figs. 3(b) and 3(c)]. In the f-FM phase [Fig. 3(c)], the splitting of band II reaches as large as ~ 70 meV for the present U_{eff} value, and the Weyl-like points are formed at $E \sim -20$ and -110 meV.

In order to quantitatively discuss their impact based on the first-principles calculation, it is necessary to determine the position of E_F . Hence, we performed high-field measurements up to 55 T using a pulsed magnet to reveal the quantum oscillation phenomena. Figure 4(a) shows the field dependence of ρ_{xx} at $T = 1.4$ K. At fields exceeding 10 T, ρ_{xx} increases almost linearly with respect to the field wherein the Shubnikov–de Haas (SdH) oscillation is superimposed (solid triangles indicate the peak positions of the oscillation). The fast Fourier transform (FFT) spectrum of $-d^2 \rho_{xx} / d(1/B)^2$ shows the clear single peak at a frequency of $B_F = 36.8$ T as shown in the inset. Figures 4(b) and 4(c) show the field dependence of resonance frequency of TDO, Δf , and the relative elastic constant, $\Delta C_{33} / C_{33} = [C_{33}(B) - C_{33}(B = 0)] / C_{33}(B = 0)$, respectively. For both physical quantities, the oscillatory structures consistent with the SdH oscillation were observed above B_c (denoted by solid triangles). Moreover, by considering that the acoustic de Haas–van Alphen

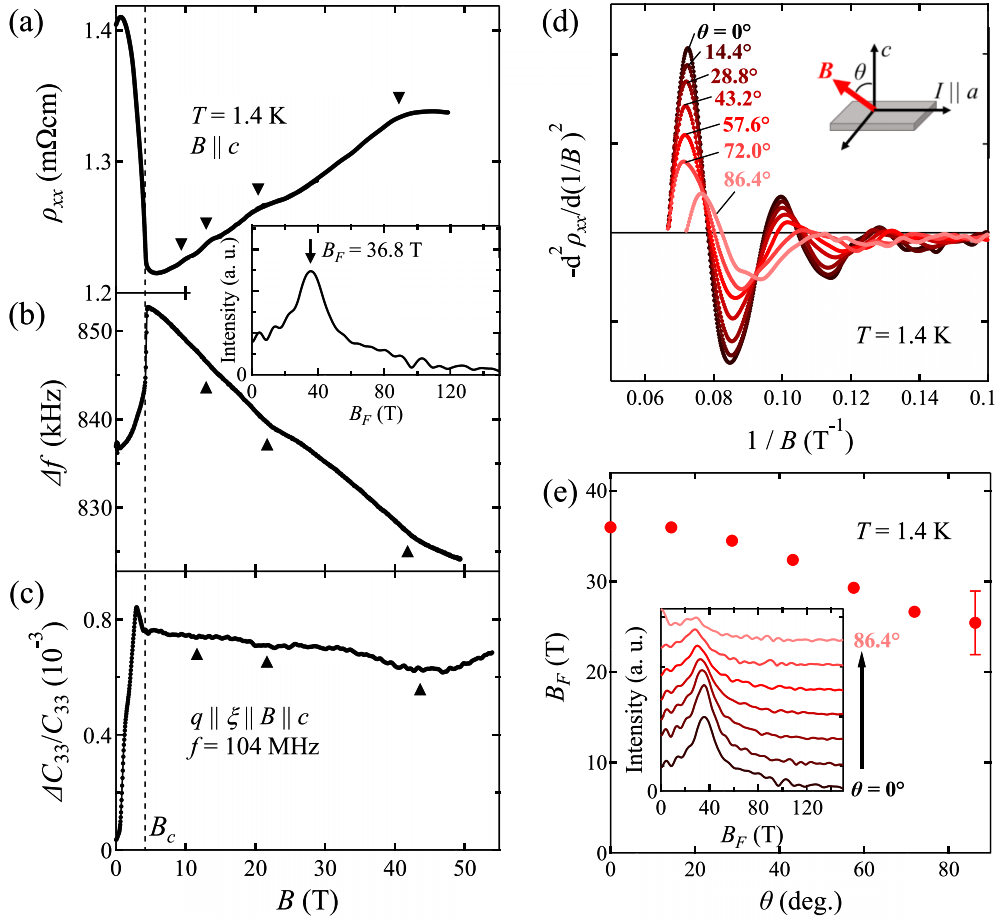


FIG. 4. (a)–(c) Field dependence of (a) ρ_{xx} , (b) resonance frequency of tunnel diode oscillator Δf , and (c) the relative change of longitudinal elastic constant $\Delta C_{33}/C_{33}$ at $T = 1.4$ K up to ~ 50 T. Triangles denote the oscillatory component. The inset shows the fast Fourier transform (FFT) spectrum of $-d^2\rho_{xx}/d(1/B)^2$ for a field of 5–15 T. q and ξ in (c) indicate the propagation and polarization direction of ultrasonic waves, respectively. (d) $-d^2\rho_{xx}/d(1/B)^2$ vs $1/B$ at various field tilt angles (θ), where θ is the angle between the c axis and magnetic field (see inset). (e) The θ dependence of oscillation frequency B_F , which is determined from the FFT spectra of $-d^2\rho_{xx}/d(1/B)^2$ shown in the inset.

effect in Fig. 4(c) is due to the Landau quantization via the electron-phonon coupling [65,66], the observed quantum oscillation should arise from a bulk band.

The quantum oscillation of the bulk origin is also supported by the dependence of B_F on the tilt angle of field. Figure 4(d) shows $-d^2\rho_{xx}/d(1/B)^2$ vs $1/B$ at $T = 1.4$ K for various θ values, where θ denotes the tilt angle with respect to the c axis (see the inset). While the amplitude of the SdH oscillation gradually decreases as θ increases, the positions of peaks and dips are almost unchanged with respect to θ , resulting in nearly θ -independent B_F [Fig. 4(e)]. This θ dependence of B_F indicates that the detected Fermi surface is three dimensional and almost isotropic [67], and it is consistent with the hole pocket at the Γ point obtained by the first-principles calculation (Fig. S4).

Finally, we estimate the position of E_F based on the quantum oscillation. Since the quantum oscillation is discernible in the f-FM phase (above 10 T), we compare the experimental result with the band structure for the f-FM phase [Fig. 3(c)]. From the experimental B_F value, the Fermi-surface cross section S_F on the $k_x k_y$ plane is estimated as $S_F = 0.352 \text{ nm}^{-2}$ at $\theta = 0^\circ$ [by Onsager's theorem, $S_F =$

$(2\pi e/\hbar)B_F]$. Theoretically, the Fermi surface on the $k_x k_y$ plane approximately consists of inner and outer surfaces, ignoring the spin splitting [inset to Fig. 3(c)]. Assuming that the observed B_F corresponds to the inner Fermi surface, E_F is located at $E = -110 \text{ meV}$ [68], and the carrier density is calculated as $n_{\text{calc}} = 1.9 \times 10^{19} \text{ cm}^{-3}$. This carrier density is in good agreement with that estimated from the Hall coefficient R_H at high magnetic field ($n_{\text{Hall}} = 2.0 \times 10^{19} \text{ cm}^{-3}$ at 2 K). Conversely, if we assume that the experimental B_F corresponds to the outer surface, then we obtain $E_F = -30 \text{ meV}$ and $n_{\text{calc}} = 1.3 \times 10^{18} \text{ cm}^{-3}$. The latter value is 1/10 lower than n_{Hall} . Therefore, the quantum oscillation should arise from the inner Fermi surface, and the resultant E_F ($= -110 \text{ meV}$) is denoted by the horizontal dashed line in Fig. 3(c).

Based on the fact that the carrier density is constant irrespective of the magnetic order, E_F was also determined for the A-AFM and canted AFM phases [dashed lines in Figs. 3(a) and 3(b)]. In the A-AFM phase, E_F is located approximately 60 meV below the Dirac point. On the other hand, in the f-FM phase, the lower-energy Weyl point, which is generated from the Dirac point by spin splitting, is located very close

to E_F . Consequently, as shown in Fig. 3(d), the calculated E_F dependence of σ_{xy}^A exhibits a clear peak around the experimental E_F value ($= -110$ meV). The peak value of σ_{xy}^A quantitatively agrees with the experimental data of EuMg_2Bi_2 [solid circle in Fig. 3(d)]. We further experimentally investigated the E_F dependence of σ_{xy}^A by synthesizing crystals with different carrier concentrations via annealing and doping (Fig. S9); The resultant σ_{xy}^A data also exhibit a peak around $E_F \sim -110$ meV [Fig. 3(d)]. Such a quantitative agreement between the calculated and experimental E_F dependence of σ_{xy}^A strongly indicates that the AHE in EuMg_2Bi_2 is explained by the intrinsic Berry curvature mechanism. These detailed analyses on E_F and σ_{xy}^A for a single-valley system should provide firm evidence of a marked impact of the emergent Weyl points on the transport phenomena.

In conclusion, we examined a band structure controllable by the magnetic order and associated large anomalous Hall effect (with a Hall angle of ~ 0.07) in the degenerate magnetic semiconductor EuMg_2Bi_2 , which exhibits the same crystal structure as the putative topological material $(\text{Sr}, \text{Ba})\text{Mg}_2\text{Bi}_2$. When the field is applied along the c axis, the bands exhibit large spin splitting due to the exchange interactions with Eu

spins, resulting in field-tunable Weyl points. Based on the experimental E_F determined from the quantum oscillation at high fields, we revealed that the low-energy Weyl points are formed very close to E_F in a forced ferromagnetic phase, which quantitatively explains the observed large anomalous Hall effect in this compound.

The authors are grateful to Y. Kohama for experimental advice. This work was partly supported by the JSPS KAKENHI (Grants No. 19H01851, No. 19K21851, No. 22H00109, No. 22J10851, and No. 21H00147) and the Asahi Glass Foundation. The x-ray diffraction experiments at KEK were performed under the approval of the Photon Factory Program Advisory Committee (Proposals No. 2018S2-006 and No. 2021S2-004). This work was carried out in part at the Center for Spintronics Research Network (CSRN), Graduate School of Engineering Science, Osaka University. This work was performed using facilities of the Institute for Solid State Physics, the University of Tokyo and the Center for Advanced High Magnetic Field Science in Osaka University under the Visiting Researcher's Program of the Institute for Solid State Physics, the University of Tokyo.

-
- [1] N. Nagaosa, T. Morimoto, and Y. Tokura, *Nat. Rev. Mater.* **5**, 621 (2020).
- [2] S. Nakatsuji, N. Kiyohara, and T. Higo, *Nature (London)* **527**, 212 (2015).
- [3] A. K. Nayak, J. E. Fischer, Y. Sun, B. Yan, J. Karel, A. C. Komarek, C. Shekhar, N. Kumar, W. Schnelle, J. Kübler, C. Felser, and S. S. P. Parkin, *Sci. Adv.* **2**, e1501870 (2016).
- [4] N. Kiyohara, T. Tomita, and S. Nakatsuji, *Phys. Rev. Appl.* **5**, 064009 (2016).
- [5] M. Ikhlas, T. Tomita, T. Koretsune, M. Suzuki, D. Nishio-Hamane, R. Arita, Y. Otani, and S. Nakatsuji, *Nat. Phys.* **13**, 1085 (2017).
- [6] L. Xu, X. Li, X. Lu, C. Collignon, H. Fu, J. Koo, B. Fauqué, B. Yan, Z. Zhu, and K. Behnia, *Sci. Adv.* **6**, eaaz3522 (2020).
- [7] T. Chen, T. Tomita, S. Minami, M. Fu, T. Koretsune, M. Kitatani, Ikhals Muhammad, D. Nishio-Hamane, R. Ishii, F. Ishii, R. Arita, and S. Nakatsuji, *Nat. Commun.* **12**, 572 (2021).
- [8] E. Liu, Y. Sun, N. Kumar, L. Muechler, A. Sun, L. Jiao, S. Yang, D. Liu, A. Liang, Q. Xu, J. Kroder, V. Süß, H. Borrmann, C. Shekhar, Z. Wang, C. Xi, W. Wang, W. Schnelle, S. Wirth, Y. Chen *et al.*, *Nat. Phys.* **14**, 1125 (2018).
- [9] Q. Wang, Y. Xu, R. Lou, Z. Liu, M. Li, Y. Huang, D. Shen, H. Weng, S. Wang, and H. Lei, *Nat. Commun.* **9**, 3681 (2018).
- [10] M. Tanaka, Y. Fujishiro, M. Mogi, Y. Kaneko, T. Yokosawa, N. Kanazawa, S. Minami, T. Koretsune, R. Arita, S. Tarucha, M. Yamamoto, and Y. Tokura, *Nano Lett.* **20**, 7476 (2020).
- [11] S. N. Guin, R. Vir, Y. Zhang, N. Kumar, S. J. Watzman, C. Fu, E. Liu, K. Manna, W. Schnelle, J. Gooth, C. Shekhar, Y. Sun, and C. Felser, *Adv. Mater.* **31**, 1806622 (2019).
- [12] K. Kim, J. Seo, E. Lee, K.-T. Ko, B. S. Kim, B. G. Jang, J. M. Ok, J. Lee, Y. J. Jo, W. Kang, J. H. Shim, C. Kim, H. W. Yeom, B. I. Min, B. Yang, and J. S. Kim, *Nat. Mater.* **17**, 794 (2018).
- [13] J. Xu, W. A. Phelan, and C. Chien, *Nano Lett.* **19**, 8250 (2019).
- [14] A. Sakai, Y. P. Mizuta, A. A. Nugroho, R. Sihombing, T. Koretsune, M. Suzuki, N. Takemori, R. Ishii, D. Nishio-Hamane, R. Arita, P. Goswami, and S. Nakatsuji, *Nat. Phys.* **14**, 1119 (2018).
- [15] S. N. Guin, K. Manna, J. Noky, S. J. Watzman, C. Fu, N. Kumar, W. Schnelle, C. Shekhar, Y. Sun, J. Gooth, and C. Felser, *NPG Asia Mater.* **11**, 16 (2019).
- [16] A. Markou, D. Kriegner, J. Gayles, L. Zhang, Y. C. Chen, B. Ernst, Y. H. Lai, W. Schnelle, Y. H. Chu, Y. Sun, and C. Felser, *Phys. Rev. B* **100**, 054422 (2019).
- [17] L. Xu, X. Li, L. Ding, T. Chen, A. Sakai, B. Fauqué, S. Nakatsuji, Z. Zhu, and K. Behnia, *Phys. Rev. B* **101**, 180404(R) (2020).
- [18] K. Sumida, Y. Sakuraba, K. Masuda, T. Kono, M. Kakoki, K. Goto, W. Zhou, K. Miyamoto, Y. Miura, T. Okuda, and A. Kimura, *Commun Mater* **1**, 89 (2020).
- [19] C. Shekhar, N. Kumar, V. Grinenko, S. Singh, R. Sarkar, H. Luetkens, S. Wu, Y. Zhang, A. C. Komarek, E. Kampert, Y. Skourski, J. Wosnitza, W. Schnelle, A. McCollam, U. Zeitler, J. Kübler, B. Yan, H.-H. Klauss, S. S. P. Parkin, and C. Felser, *Proc. Natl. Acad. Sci. USA* **115**, 9140 (2018).
- [20] T. Suzuki, R. Chisnell, A. Devarakonda, Y.-T. Liu, W. Feng, D. Xiao, J. W. Lynn, and J. G. Checkelsky, *Nat. Phys.* **12**, 1119 (2016).
- [21] K. S. Takahashi, H. Ishizuka, T. Murata, Q. Y. Wang, Y. Tokura, N. Nagaosa, and M. Kawasaki, *Sci. Adv.* **4**, eaar7880 (2018).
- [22] Y. Xu, L. Das, J. Z. Ma, C. J. Yi, S. M. Nie, Y. G. Shi, A. Tiwari, S. S. Tsirkin, T. Neupert, M. Medarde, M. Shi, J. Chang, and T. Shang, *Phys. Rev. Lett.* **126**, 076602 (2021).
- [23] X. Cao, J. Yu, P. Leng, C. Yi, Y. Yang, S. Liu, L. Kong, Z. Li, X. Dong, Y. Shi, J. Zang, and F. Xiu, *Phys. Rev. Res.* **4**, 023100 (2022).
- [24] J.-R. Soh, F. de Juan, M. G. Vergniory, N. B. M. Schröter, M. C. Rahn, D. Y. Yan, J. Jiang, M. Bristow, P. Reiss, J. N. Blandy,

- Y. F. Guo, Y. G. Shi, T. K. Kim, A. McCollam, S. H. Simon, Y. Chen, A. I. Coldea, and A. T. Boothroyd, *Phys. Rev. B* **100**, 201102(R) (2019).
- [25] J.-R. Soh, C. Donnerer, K. M. Hughes, E. Schierle, E. Weschke, D. Prabhakaran, and A. T. Boothroyd, *Phys. Rev. B* **98**, 064419 (2018).
- [26] H. Su, B. Gong, W. Shi, H. Yang, H. Wang, W. Xia, Z. Yu, P. Guo, J. Wang, L. Ding, L. Xu, X. Li, X. Wang, Z. Zou, N. Yu, Z. Zhu, Y. Chen, Z. Liu, K. Liu, G. Li *et al.*, *APL Mater.* **8**, 011109 (2020).
- [27] M. Ohno, S. Minami, Y. Nakazawa, S. Sato, M. Kriener, R. Arita, M. Kawasaki, and M. Uchida, *Phys. Rev. B* **105**, L201101 (2022).
- [28] A. H. Mayo, H. Takahashi, M. S. Bahramy, A. Nomoto, H. Sakai, and S. Ishiwata, *Phys. Rev. X* **12**, 011033 (2022).
- [29] A. F. May, M. A. McGuire, D. J. Singh, R. Custelcean, and G. E. Jellison, Jr., *Inorg. Chem.* **50**, 11127 (2011).
- [30] Z. Zhang, R. Zhang, X. Li, K. Koepf, Y. Yao, and H. Zhang, *J. Phys. Chem. Lett.* **9**, 6224 (2018).
- [31] E. K. Petrov, I. V. Silkin, Y. M. Koroteev, and E. V. Chulkov, *JETP Lett.* **105**, 502 (2017).
- [32] D. Takane, Y. Kubota, K. Nakayama, T. Kawakami, K. Yamauchi, S. Souma, T. Kato, K. Sugawara, S. Ideta, K. Tanaka, M. Kitamura, K. Horiba, H. Kumigashira, T. Oguchi, T. Takahashi, K. Segawa, and T. Sato, *Sci. Rep.* **11**, 21937 (2021).
- [33] M. Marshall, I. Pletikosić, M. Yahyavi, H. Tien, T. Chang, H. Cao, and W. Xie, *J. Appl. Phys.* **129**, 035106 (2021).
- [34] S. Pakhira, M. A. Tanatar, and D. C. Johnston, *Phys. Rev. B* **101**, 214407 (2020).
- [35] S. Pakhira, T. Heitmann, S. X. M. Riberolles, B. G. Ueland, R. J. McQueeney, D. C. Johnston, and D. Vaknin, *Phys. Rev. B* **103**, 024408 (2021).
- [36] T. Coffey, Z. Bayindir, J. F. DeCarolis, M. Bennett, G. Esper, and C. C. Agosta, *Rev. Sci. Instrum.* **71**, 4600 (2000).
- [37] T. K. Fujita, M. Yoshizawa, R. Kamiya, H. Mitamura, T. Sakakibara, K. Kindo, F. Iga, I. Ishii, and T. Suzuki, *J. Phys. Soc. Jpn.* **80**, SA084 (2011).
- [38] A. V. Krukau, O. A. Vydrov, A. F. Izmaylov, and G. E. Scuseria, *J. Chem. Phys.* **125**, 224106 (2006).
- [39] G. Kresse and D. Joubert, *Phys. Rev. B* **59**, 1758 (1999).
- [40] A. I. Liechtenstein, V. I. Anisimov, and J. Zaanen, *Phys. Rev. B* **52**, R5467 (1995).
- [41] S. L. Dudarev, G. A. Botton, S. Y. Savrasov, C. J. Humphreys, and A. P. Sutton, *Phys. Rev. B* **57**, 1505 (1998).
- [42] It was found that the magnitude and sign of the spin splitting of bands is dependent on U_{eff} [Fig. S8(a)]. We here determined the U_{eff} value, so that the calculated Fermi energy dependence of anomalous Hall conductivity reproduces the experimental results [Figs. S8(b) and S8(c)].
- [43] G. Kresse and J. Hafner, *Phys. Rev. B* **47**, 558 (1993).
- [44] G. Kresse and J. Hafner, *Phys. Rev. B* **49**, 14251 (1994).
- [45] G. Kresse and J. Furthmüller, *Comput. Mater. Sci.* **6**, 15 (1996).
- [46] G. Kresse and J. Furthmüller, *Phys. Rev. B* **54**, 11169 (1996).
- [47] N. Marzari and D. Vanderbilt, *Phys. Rev. B* **56**, 12847 (1997).
- [48] I. Souza, N. Marzari, and D. Vanderbilt, *Phys. Rev. B* **65**, 035109 (2001).
- [49] G. Pizzi *et al.*, *J. Phys.: Condens. Matter* **32**, 165902 (2020).
- [50] See Supplemental Material at <http://link.aps.org/supplemental/10.1103/PhysRevB.107.L121112> for details of the experimental and computational methods, which includes Refs. [51–56].
- [51] M. Kawamura, *Comput. Phys. Commun.* **239**, 197 (2019).
- [52] S. S. Tsirkin, *npj Comput. Mater.* **7**, 33 (2021).
- [53] D. Destraz, L. Das, S. S. Tsirkin, Y. Xu, T. Neupert, J. Chang *et al.*, *npj Quantum Mater.* **5**, 5 (2020).
- [54] K. Imasato, C. Fu, Y. Pan, M. Wood, J. Kuo, C. Felser, and G. Snyder, *Adv. Mater.* **32**, 1908218 (2020).
- [55] N. Kanazawa, Y. Onose, T. Arima, D. Okuyama, K. Ohoyama, S. Wakimoto, K. Kakurai, S. Ishiwata, and Y. Tokura, *Phys. Rev. Lett.* **106**, 156603 (2011).
- [56] M. Lee, Y. Onose, Y. Tokura, and N. P. Ong, *Phys. Rev. B* **75**, 172403 (2007).
- [57] H. Masuda, H. Sakai, M. Tokunaga, Y. Yamasaki, A. Miyake, J. Shiogai, S. Nakamura, S. Awaji, A. Tsukazaki, H. Nakao, Y. Murakami, T. Arima, Y. Tokura, and S. Ishiwata, *Sci. Adv.* **2**, e1501117 (2016).
- [58] H. Masuda, H. Sakai, H. Takahashi, Y. Yamasaki, A. Nakao, T. Moyoshi, H. Nakao, Y. Murakami, T. Arima, and S. Ishiwata, *Phys. Rev. B* **101**, 174411 (2020).
- [59] S. Pakhira, F. Islam, E. O’Leary, M. A. Tanatar, T. Heitmann, L. L. Wang, R. Prozorov, A. Kaminski, D. Vaknin, and D. C. Johnston, *Phys. Rev. B* **106**, 024418 (2022).
- [60] At high temperatures ($\gg T_N$), where the normal component is dominant, the field dependence of Hall resistivity is almost linear (see Fig. S7 in Supplemental Material [60]). This means that the multiband effect is negligibly small in this material.
- [61] The fitting below B_c is improved by considering the dependence of ρ_{yx}^A on ρ_{xx} (i.e., $\rho_{yx}^A \propto \rho_{xx}^2 M$), characteristic of the intrinsic mechanism (see Fig. S4).
- [62] N. Nagaosa, J. Sinova, S. Onoda, A. H. MacDonald, and N. P. Ong, *Rev. Mod. Phys.* **82**, 1539 (2010).
- [63] S. Onoda, N. Sugimoto, and N. Nagaosa, *Phys. Rev. Lett.* **97**, 126602 (2006).
- [64] H. Masuda, H. Sakai, M. Tokunaga, M. Ochi, H. Takahashi, K. Akiba, A. Miyake, K. Kuroki, Y. Tokura, and S. Ishiwata, *Phys. Rev. B* **98**, 161108(R) (2018).
- [65] R. Kurihara, A. Miyake, M. Tokunaga, Y. Hirose, and R. Settai, *Phys. Rev. B* **101**, 155125 (2020).
- [66] M. Kataoka and T. Goto, *J. Phys. Soc. Jpn.* **62**, 4352 (1993).
- [67] D. Shoenberg, *Magnetic Oscillations in Metals* (Cambridge University Press, Cambridge, U.K., 1984).
- [68] We determined the Fermi energy (E_F) in Figs. 3(b) and 3(c) so that the experimental Fermi-surface cross section is consistent with the averaged cross section of the two valence bands labeled as II.